Electronic Supplementary Material (ESI) for Nanoscale.

Tuning Fermi level with topological phase transition by internal strain in topological insulator Bi_2Se_3 thin film

Tae-Hyeon Kim[1], KwangSik Jeong[1], Byung Cheol Park[1], Hyejin Choi[1], Sang Han Park[1], Seonghoon Jung[2], Jaehun Park[2], Kwang-Ho Jeong[1], Jeong Won Kim[3], Jae Hoon Kim[1], and Mann–Ho Cho[1*]

[1] Institute of Physics and Applied Physics, Yonsei University, Republic of Korea

[2] Pohang Accelerator Laboratory, POSTECH, Pohang 790-784, Republic of Korea

[3] Division of Industrial Metrology, Korea Research Institute of Standards and Science, Republic of Korea

*mh.cho@yonsei.ac.kr

S1. Strain generation in self-ordered grown thin film.

The strain is generated by volume shrinkage through the diffusion process during the annealing treatment. As we described in our original manuscript on line 10, page 3, the self-ordering process for a single crystalline Bi_2Se_3 film through a short range diffusion, which can overcome the synthetic limitations of slow diffusion rates in solid-state reactions (Ref. 22) requires the formation of alternate layers with Bi atoms and excess Se atoms. In this process, nearly 78% of the deposited Se atoms diffuse through the surface along the c-axis during the subsequent thermal processing. As a result of Se diffusion, the Bi_2Se_3 film shrank to only about 45% of its original volume. In Fig. S1 below, we show a schematic of strain generation with volume shrinkage through the diffusion of Se atoms.

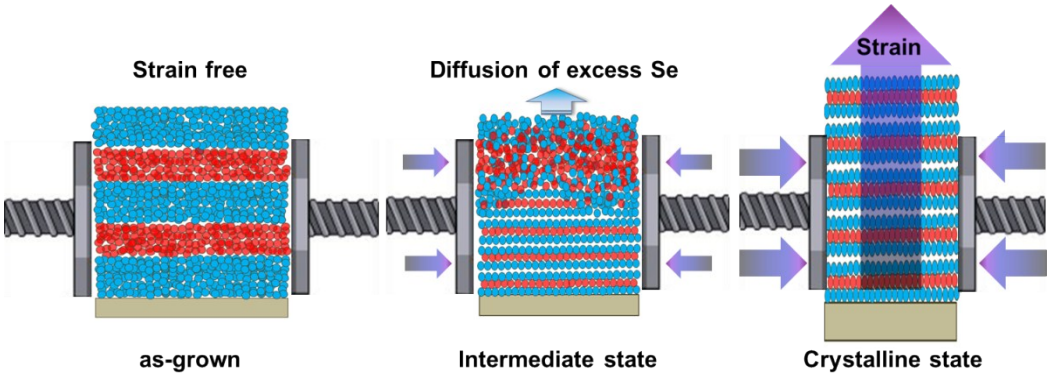

Figure S1 | In the annealing process, 78% of the deposited Se atoms diffuse through the surface. As a result, the film shrinks to about 45% of its original volume.

To clarify the sources of strain in our thin film, we performed additional experiments using graphene as the substrate. The unit cell of Bi_2Se_3 has lattice constants a~4.14 Å, c~28.636 Å. Graphene exhibits a hexagonal symmetry with the lattice constant a=2.46 Å. The length of the C-C bond in graphene is ~1.42 Å and the hexagonal periodicity of the graphene surface along which the Bi_2Se_3 aligns is d=4.26 Å, which has a lattice mismatch of ~2.9% with Bi_2Se_3. Such a small lattice mismatch should introduce significant

strain in Bi_2Se_3 film under 2~3 QL (Ref. 38, 39, 40). Since the lattice mismatch-induced tensile strain in the ab-axis (from Ref. 38) is totally different from our experiment result in Fig.4 (SAXS), we were able to define the prevalent source of strain from direct comparison between Fig. 4c (SAXS) and Fig. S2 below.

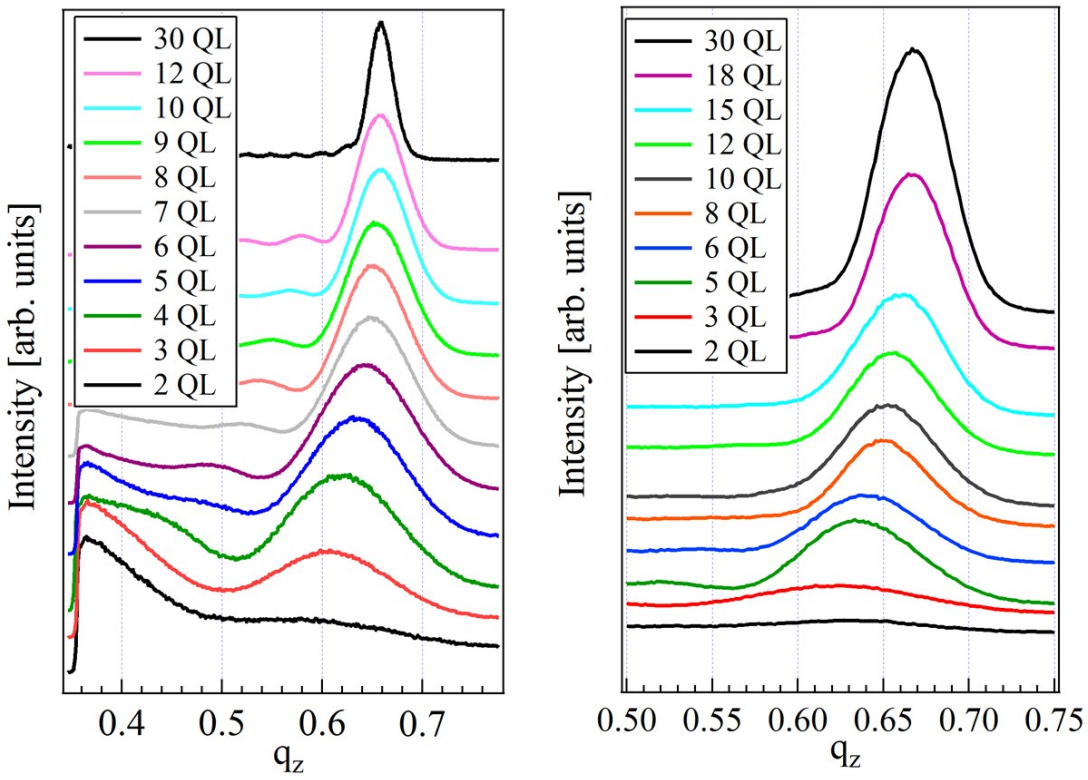

Figure S2 | Out-of-plane scan profiles for the Bi_2Se_3 thin films obtained from the GISAXS patterns. Bi_2Se_3 / SiO_2(native oxide) / Si substrate. (Left) A difference between 30QL (9.54Å) and 3 QL (10.27Å) is 7.11 %. Bi_2Se_3 / Graphene substrate. (Right) A difference between 30QL (9.54Å) and 3QL (10.05Å) is 5.07%.

D-spacing values in SAXS result of Bi_2Se_3 / SiO_2 substrate are 9.54Å, 9.91Å and 10.27Å at 30 QL, 5 QL and 3 QL film, respectively. The results of Bi_2Se_3 / Graphene substrate are 9.54Å, 9.87Å and 10.05Å at 30 QL, 5 QL and 3 QL film respectively. The results indicate that the prevalent source of strain, which

acts as a tensile force in the c-axis and a compressive force in the ab-axis, is volume shrinkage followed by diffusion of Se. Maximum difference between SiO_2 substrate and graphene substrate means interfacial strain at Bi_2Se_3/Graphene role as a weak anti-strain effect in this case, which is tensile strain in the ab-axis, as reported before (Ref. 38).

S2. Sample characterization.

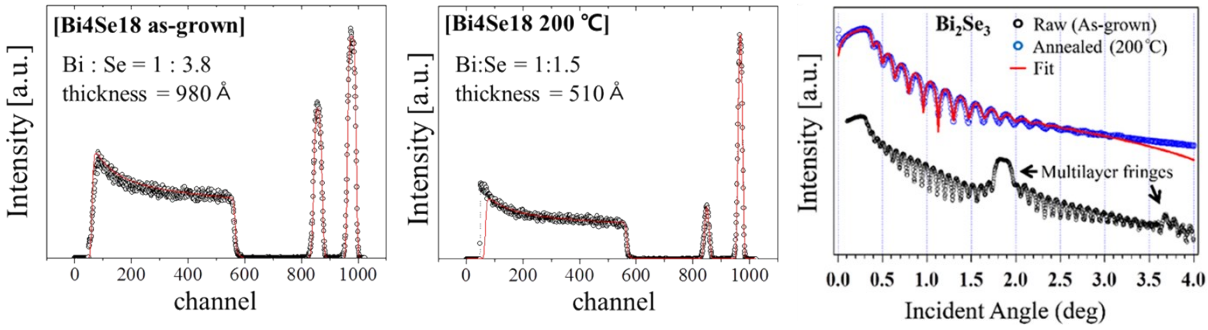

Figure S3 | RBS spectra of alternate layered films composed of individual layers of [Bi(4.9 Å)/Se(18.5 Å)] for an as-grown Bi4Se18 film (980 Å) and the film after annealing at 200 ℃ (left and middle). The composition and thickness after annealing are [Bi(1):Se(1.5)] and 510 Å, respectively. X-ray reflectivity of the multilayer film (right) (Ref. 21). The definition of thickness and composition ratio using Rutherford backscattering and X-ray reflectivity was performed in our previous work within ±0.1% of error. [1]

To determine thickness of our film, we carried out Rutherford backscattering spectroscopy and X-ray reflectivity. From the RBS spectra (from Fig. S3), the ratio of Bi to Se in the film and the film thickness was determined. The ratio of Bi to Se was changed from 1:3.8 (amorphous) to 1:1.5 (crystallized) and the film thickness changed from 980 to 510 Å. From the measured thickness and composition ratios of Se and Bi, we were able to extract the alternate layer thickness for Bi (4.86Å) and Se (18.46Å) in the as-grown film. To confirm the designed layer thickness and roughness, X-ray reflectivity was also measured. The

as-grown film has a critical angle of 0.31° and two Bragg-like diffraction peaks at 1.82° and 3.68°, which are due to the repeated multilayer structure. From the critical angle and repeated fringes, it was possible to evaluate the density (6.1 g/cm^3) and the periodic cycle of the alternating two layers (23.3 Å). The grown layer thickness is consistent with the designed layer thickness (4.86 Å+18.46 Å= 23.32Å) as we referred above. Also we conclude that the dominant sources of error which affect thickness definition come from fitting process arising from the difference in the RBS spectra fitting results and the X-ray reflectivity results. A maximum deviation of 0.02 Å leads to a 0.08% error for the results.

Well-ordered Bi_2Se_3 layers and distinct interfaces without any imperfections were confirmed by TEM analysis (Ref 21, 25). In order to confirm the uniformity of the film, we observed several interface areas with high magnification (the third row). The TEM images show that the Bi_2Se_3 thin film with a high-quality single crystal structure is well formed over a wide region even on an imperfectly-defined amorphous interface layer (Ref 21, 25).

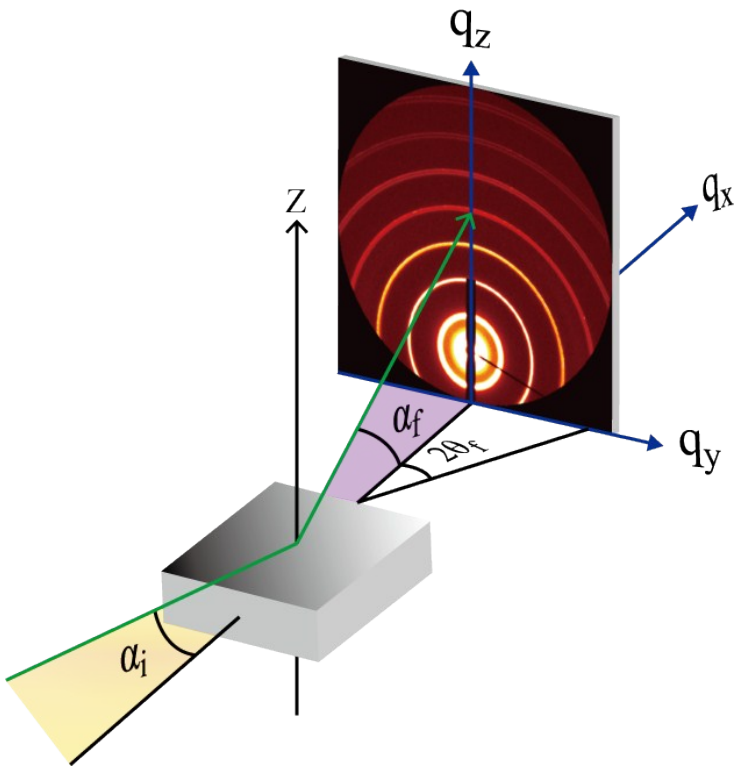

Figure S4 | Schematic of SAXS measurements.

Figure S4 shows the method used for the SAXS measurements and a typical SAXS pattern of silver behenate. Since SAXS measurements require accurate calibration determining the sample-to-detector distance, we used silver behenate as a reference to compute the exact value for q (reciprocal-space lengths) for the image on an area detector.

S3. Phonon vibration shifts with stress.

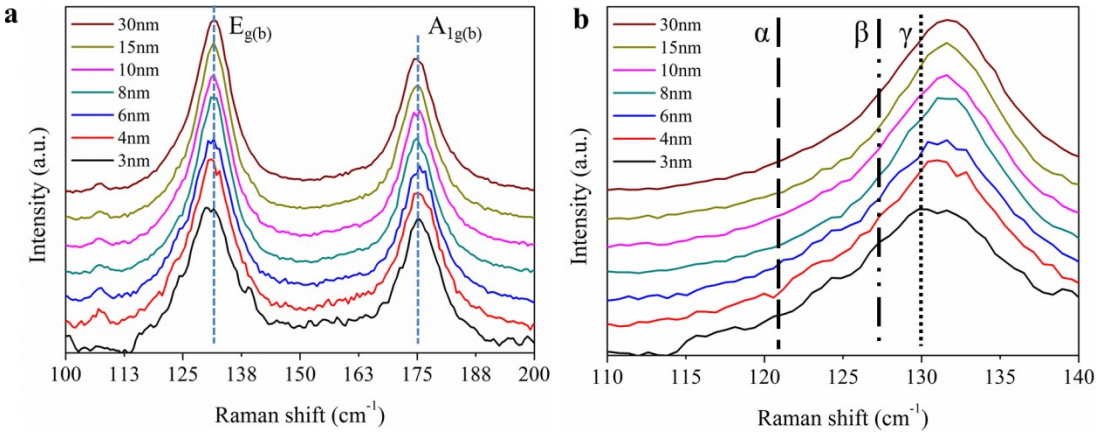

Figure S5 | Raman spectra of few QL Bi_2Se_3 thin films and analysis. a, Raman shifts of Bi_2Se_3 thin films with different thicknesses and **b,** Raman spectra near $E_{g(b)}$ mode. Each dotted line α, β and γ means predicted peak position of Bi_2Se_3 with significant tensile stress[2], that of Bi_2Se_3 without any stress (only with thickness decreasing effect) and that of Bi_2Se_3 with compressive stress, respectively.

To study the detailed properties of the strained Bi_2Se_3 thin film, we investigated the phonon properties with in-plane and out-of-plane vibration directions using Raman spectroscopy. The Raman spectra of Bi_2Se_3 thin films in Figure S6 showed two characteristic peaks at 130 and 175 cm^{-1} with a symmetric Lorentzian profile in all Bi_2Se_3 films, which corresponds to in-plane ($E_{g(b)}$) and out-of-plane

vibrational modes ($A_{1g(b)}$)[3, 4], respectively. Figure S5(b) presents the expected $E_{g(b)}$ peak position in various cases: i. e., with tensile stress, without any stress and with compressive stress. In case of tensile stress, it was already reported in *Nano lett*. that downward shift of $E_{g(b)}$ mode exits under significant tensile stress.[2] For the non-stress case, it was known that the selection rule is relaxed due to symmetry breaking based on the translational symmetry for low dimensional structures such as spherical nanocrystals or thin films. The relaxed selection rule causes red shifting about 4 cm^{-1} from the normal bulk phonon peak position,[5, 6,7] just as described in our phonon calculation results (Fig. S9), too. Only a position γ matches our result, which indicates in-plane compressive stress determines our $E_{g(b)}$ position. Comparison between predicted value of $E_{g(b)}$ vibration mode in each case and experimental data is plotted in Fig S6(c).

Another interesting finding is the nearly constant peak position of the out-of-plane vibration modes $A_{1g(b)}$ with decreasing thickness. Consider that the phonon softening effect due to a reduction of interlayer interaction[6] exists in a few quintuple layer Bi_2Se_3, the peak positons of $A_{1g(b)}$ can be only comprehended with stress in the c-axis of Bi_2Se_3 film. Since longitudinal vibration modes (A_g mode) in a rhombohedral crystal structure under tensile stress have a tendency to shift to a higher frequency[8] compared with those in zinc blende crystal structures[9], the tensile stress which cancel out phonon softening effect can be expected in our film. The tensile stress factor was already proved in results of our SAXS measurement (Fig. 4). To investigate the effect of tensile stress with the c-axis direction in our Bi_2Se_3 film in more detail, THz-TDS and the *ab-initio* calculations were carried out.

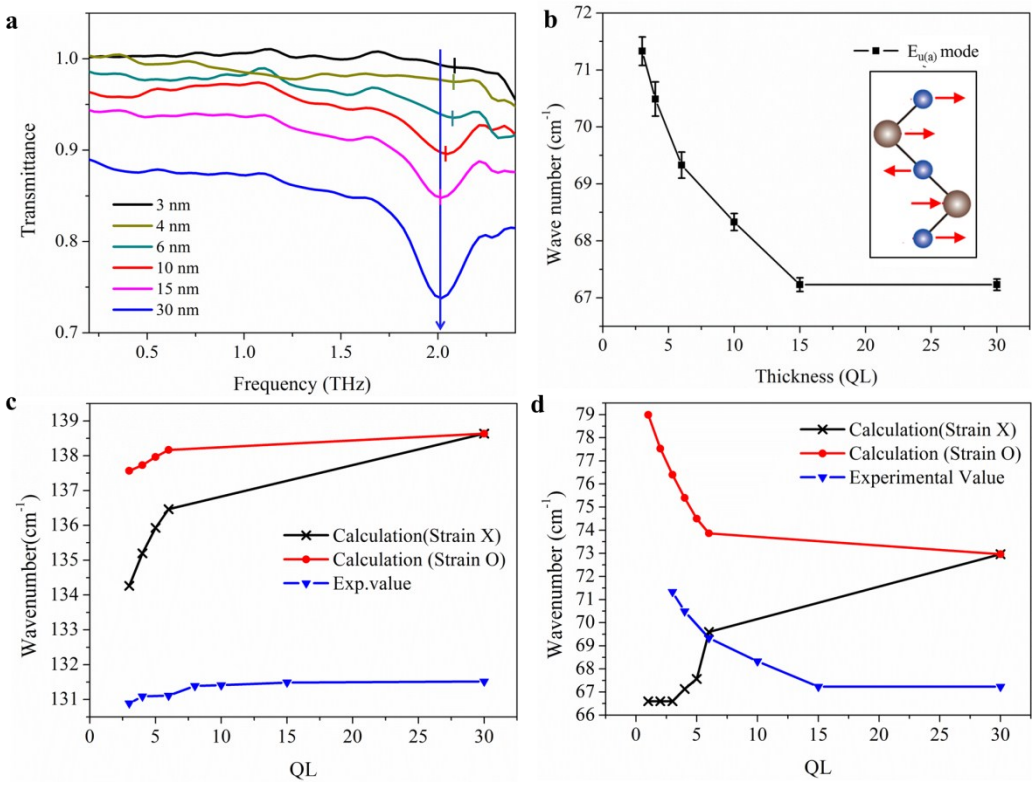

Figure S6 | THz-time domain spectroscopy of a Bi_2Se_3 thin film and calculated values. a, Measured transmittance of Bi_2Se_3 thin film for different thicknesses as a function of frequency. Bulk phonon mode of each film is marked as line. **b,** Plot of the $A_{1g(a)}$ mode frequency versus thickness. **c,d,** Evolution of the $E_{g(b)}$ mode frequencies with the calculation result as a function of thickness and that of $E_{u(a)}$ mode frequencies. The above data clearly proves that compressive stress is a key point in understanding in-plane vibration mode shifts.

In order to more closely investigate the tensile stress effect in the in-plane, we used terahertz time domain spectroscopy (THz-TDS). The transmission data in Fig. S6(a) is made up of two parts of the frequency region. One is the low frequency region associated with the free-carrier transport properties and another is the absorption peak (infra active $E_{u(a)}$ mode) at approximately 2.1 THz (~70 cm^{-1})[3, 6] corresponding to an optical phonon caused by the interaction of charged particles and electrons. The changes in the absorption peaks in Fig. S6(a), which are marked by lines in colors, show that the crystal

structure undergoes structural deformation. In particular, the degree of the characteristic vibration mode shift is dependent on the thickness of Bi_2Se_3: i.e., the vibration mode of 67.23 cm^{-1} in a 30 QL gradually increases up to 71.33 cm^{-1} at 3 QL. As shown in Fig. S6(b), the $E_{u(a)}$ vibration mode shows a nearly constant value between 30 QL to 15 QL. However, a pronounced blue shift up to 4.1 cm^{-1} was generated under 10 QL. The blue shifts in the $E_{u(a)}$ vibration mode indicate significant compressive stress in in-plane exists under 6 QL which is consistent with the tensile stress in the out-of plane direction shown as SAXS profile.

In addition, through a comparison between change of $E_{u(a)}$ mode (Fig. S6) and $E_{g(b)}$ mode (Fig. S5), we could estimate stress-vulnerability of each vibration mode. There is a significant difference between the shifted positions of the $E_{g(b)}$ mode and $E_{u(a)}$ mode, i.e., the shift in $E_{u(a)}$ is relatively high between 3 QL and 30 QL, compared to that of $E_{g(b)}$ ($E_{u(a)}$: 4.1 cm^{-1}, $E_{g(b)}$: 0.63 cm^{-1}). The results indicate that the stress factor is more effective in the $E_{u(a)}$ mode than in the $E_{g(b)}$ mode. The difference in $E_{u(a)}$ and $E_{g(b)}$ modes originates from vibration in the opposite direction between two neighboring quintuple layers. Since the $E_{u(a)}$ mode has in-phase vibrations of the outer Bi-Se pairs, it can be concluded that compressive stress in the in-plane direction results in a significant blue shift of $E_{u(a)}$ modes, unlike in the $E_{g(b)}$ modes.

Figure S6(c) and (d) show the phonon shifts depending on the thickness of the film. Calculated phonon dispersion data vary with thickness is listed in supplementary data S8. The relationship between the lattice constants change caused by stress with the phonon frequencies is in good agreement with experimental measurements. In figure S6(c), Considering the shift in the experimental data for the phonon modes between 30 QL (nearly bulk) and 3 QL films, the change in the calculation values associated with strain effect exhibiting slight red shift is relatively consistent with the experimental data, compared with the calculation values for an unstrained case showing substantial red shifting. The difference between the strained and unstrained results reflects the strong thickness effect (red shifting) and relatively small stress effect (blue shifting) for the in-plane vibration modes in 3QL film. Figure

S6(d) presents information concerning the evolution of the $E_{u(a)}$ mode frequencies in Bi_2Se_3 films as a function of film thicknesses. It is evident that the $E_{u(a)}$ modes are affected by stress factors. Both results indicate that stress in the crystal structure induces a deformation of lattice constants and phonon frequency.

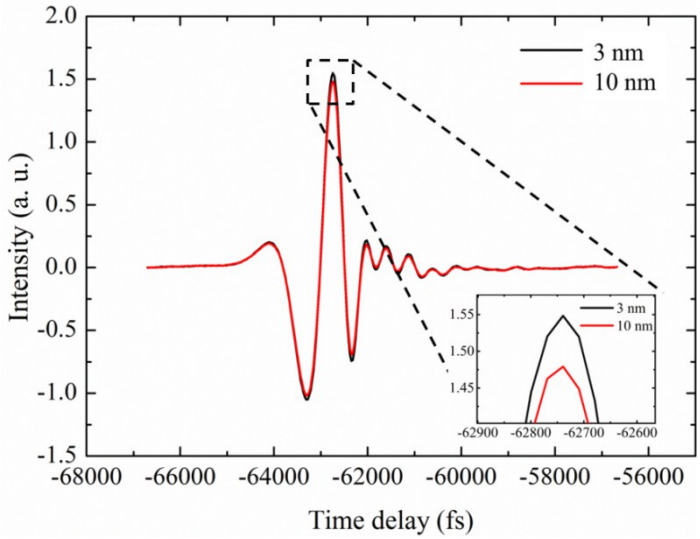

Figure S7 | Transmitted THz pulses through the Bi_2Se_3 thin film. An increasing of transmitted THz signal owing to decrease of sample thickness from 10 QL to 3 QL is presented in the inset graph.

S4. *Ab-initio* calculations.

Table S1 | Calculation details of the strained Bi_2Se_3.

QL	Stress (GPa)	Lattice x (A)	Strain (%)	Z initial	Z End	Spacing Z	Delta Z (%)

1	-1.594	3.663591	-11.11443499	0.4759	0.5444	0.0685	11.56351792
2	-2.419	3.743534	-9.174868391	0.4173	0.6027	0.1854	9.899229401
3	-2.377	3.849998	-6.591852767	0.3416	0.6158	0.2742	7.910271547
4	-3.28	3.850536	-6.578799882	0.2869	0.6938	0.4069	5.169294391
5	-2.339	3.951184	-4.136891288	0.2335	0.7478	0.5143	3.148816687
6	-2.218	3.985351	-3.307936009	0.2189	0.8221	0.6032	2.571428571

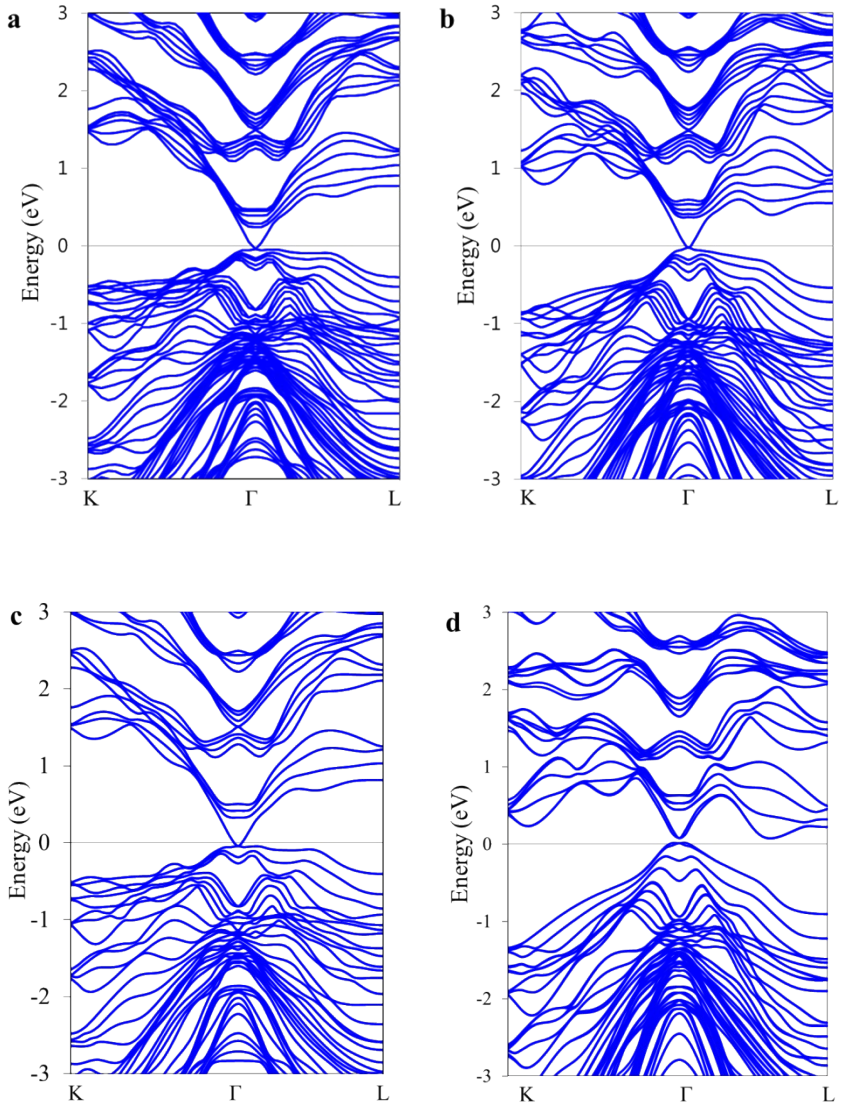

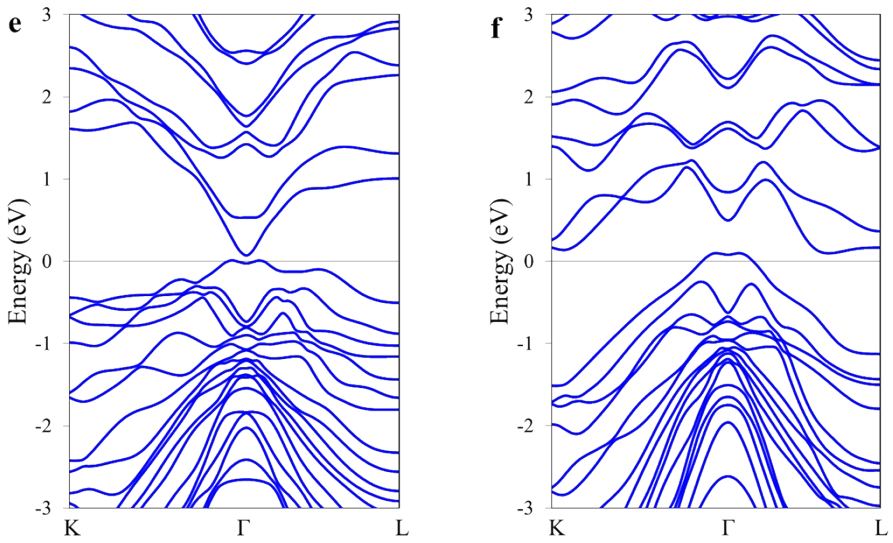

Fig S8 | Calculated band structure with SOC for a, unstrained 6 QL, **b,** strained 6 QL, **c,** unstrained 4 QL, **d,** strained 4 QL, **e,** unstrained 2 QL, **f,** and strained 2 QL Bi_2Se_3.

We carried out detailed calculations of the band structures and phonons dispersions for Bi_2Se_3 films with various thicknesses (2, 3, 4, 5, and 6 QL) and in bulk materials, with and without strain. The calculated band gap of Bi_2Se_3 with spin orbit interaction is 0.3 eV, which is consistent with the other reported calculations and experimental data.[10-14] The calculated band structure of the unstrained 6 QL Bi_2Se_3 film which show a clear topologically protected surface state is nearly the same as that of a previously reported bulk system.[14] We were able to confirm that both the strain effect and the decreasing thickness effect are important for producing unique band structure and phonon properties in Bi_2Se_3 thin films. There are clear differences between strained and unstrained Bi_2Se_3 films. Each trivial band gap of unstrained 6 QL and strained 2 QL are 0.26 eV and 1.08 eV, respectively.

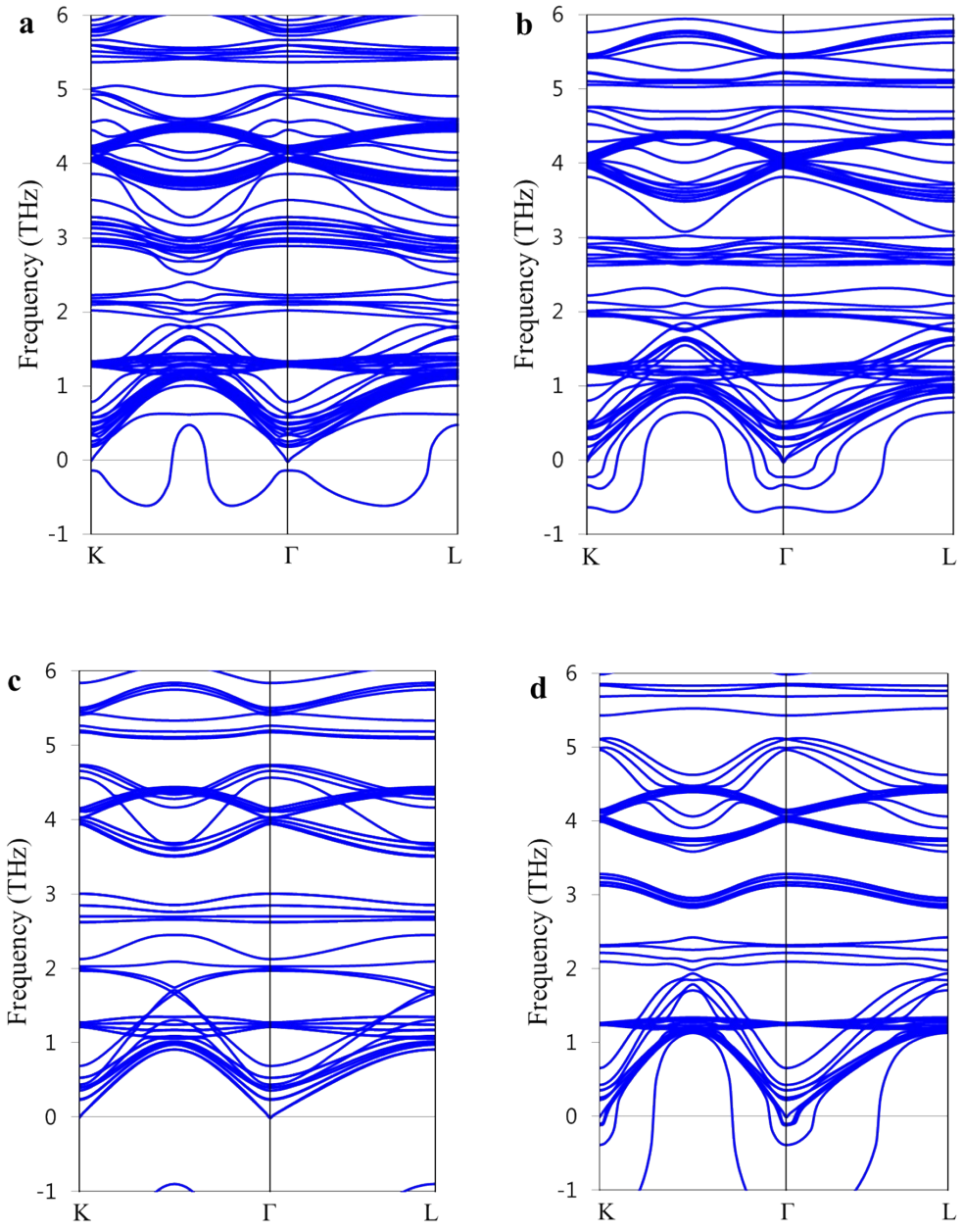
a
b
c
d
Frequency (THz)
6
5
4
3
2
1
0
-1
K
Γ
L

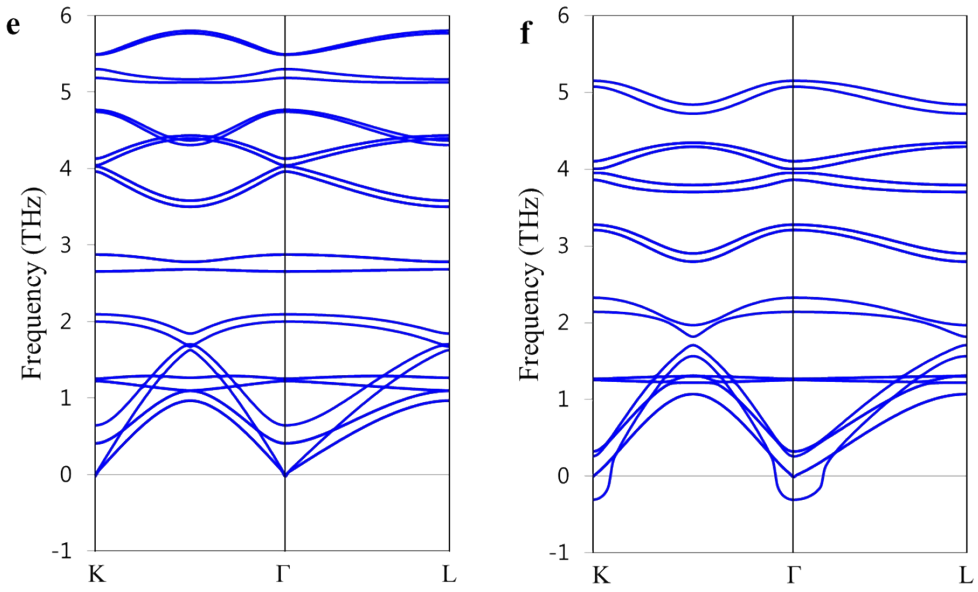

Figure S9 | Calculated phonon dispersion data. a, unstrained 6 QL, **b,** strained 6 QL, **c,** unstrained 4 QL, **d,** strained 4 QL, **e,** unstrained 2 QL, **f,** and strained 2 QL Bi_2Se_3.

S5. Stricture stability of strained Bi2Se3.

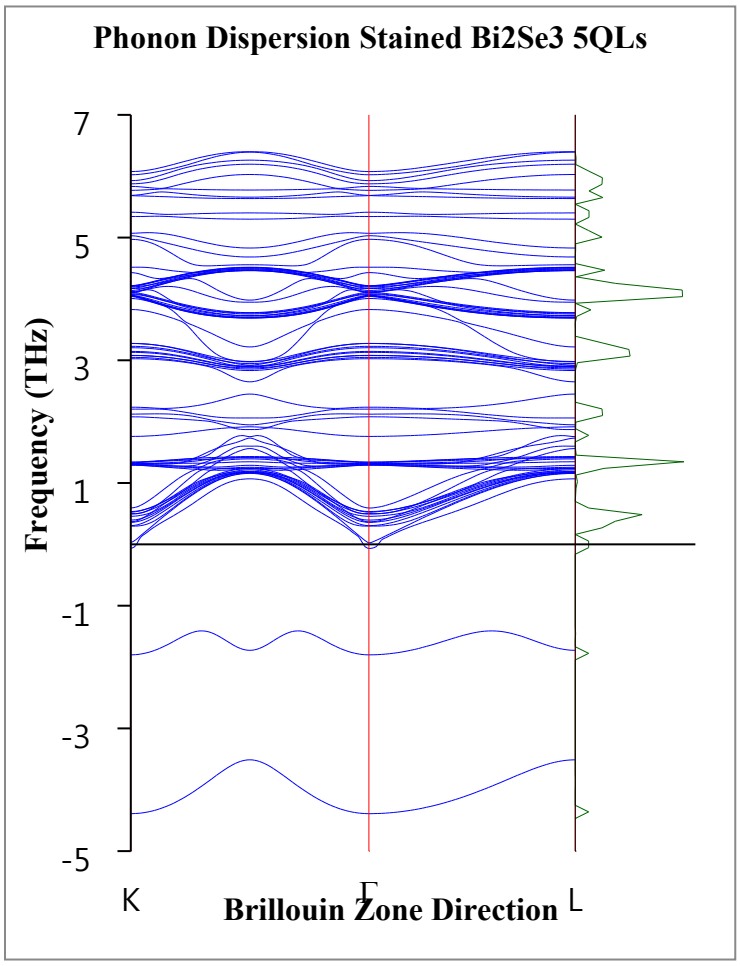

Figure S10 | Calculated phonon dispersion and density of states. for strained 5 QL Bi_2Se_3.

The Imaginary frequency of phonon means the gain in structure energy with distortion. Since a strained structure is expanded from its own stable structure, compressive atomic displacement results in a system energy. Therefore, negative phonon states are generated in strained systems. Research dealing with the relationship between a negative phonon and structure instability has been reported. By this meaning, with more states in a negative frequency phonon, the system tends to becomes unstable[15, 16]. The calculated phonon density of states for strained 5QLs Bi2Se3 is presented in figure S10. As shown in the figure, there are only two phonon dispersion bands in the negative value range which is very small, compared to the number of positive phonon states. Therefore, although stained Bi2Se3 has instability due

to a deformed stable structure in the calculation result, this instability is not sufficiently large to break or change the phase of the Bi2Se3 structure.

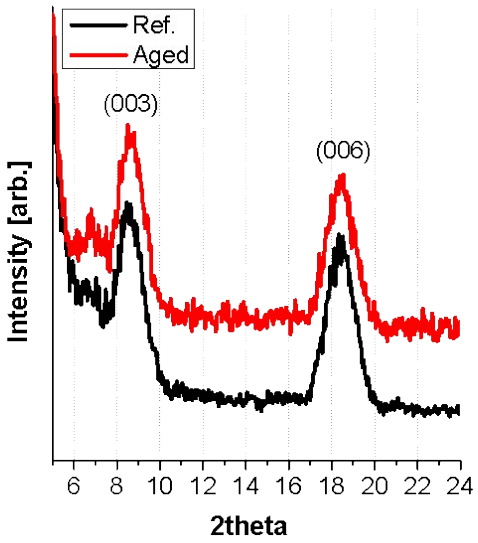

Bi2Se3	2Theta	d-spacing	strain [%]
3QL	(003)	(003)	(003)
Ref.	8.606	10.267	**7.579**
Aged	8.635	10.232	**7.220**

Figure S11. XRD spectra for fresh and aged Bi_2Se_3

To experimentally confirm the structural stability, we measured XRD for Bi2Se3 that had been aged for 1 month and fresh Bi2Se3. As shown in supporting figure S11 there was no significant change in the peak for the (003) signal which is positioned near 8.6 degrees. The strain of the aged sample is slightly changed by only 0.3%, which is within the error range of XRD. This result indicates that the strained Bi2Se3 structure is very stable.

S6. Strain-engineering of Bi_2Se_3

As shown in supporting figure S13, strained 4QLs or 5QLs Bi2Se3 show large Rashba splitting. This Rashba splitting is not observed in un-strained Bi2Se3. Due to spin flip scattering, Rashba splitting

which is the separation of up and down spin band, induces spin phase change. The amount of spin phase change is following equation[17]

$\Delta K_{rf} \times L$

Where is band splitting in the k-space by Rashba splitting and L is the channel length. Using this processional phase shift for injected electron, controllable Rashiba splitting can be used in a spin-device[18]

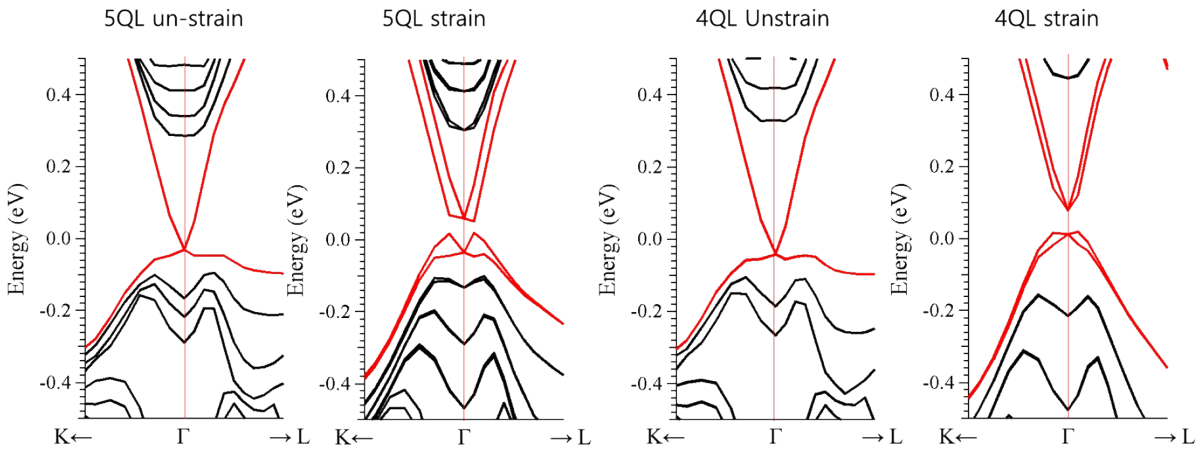

Figure S13 | Strain induced Rashba splitting in 5QL and 4QL system.

In general, strain can be changed with growth conditions such as the annealing temperature, annealing time and the composition of each layer. We conducted temperature dependent Rs measurements to determine the crystallization temperature. The thickness is around 50nm (21 multilayers). At a temperature of around 175℃, films are nearly crystallized and at temperatures over 200℃, the films are fully crystallized. Crystalline structures are maintained at the 250℃ without any changing or breaking in crystalline phase. Thus, we used annealing temperatures in the range from 200℃ to 250℃. To verify the effect of annealing conditions on the magnitude of the strain, we conducted GISAXS measurements for the annealed samples at the temperature of 250℃ as shown in figure S14. The q-value of the sample annealed at the 250℃ is 0.616 Å-1, indicating that the induced strain of 6.823

%. Considering that the strain of the sample annealed at 200C is 7.11 %, there is no significant change in the strain with the control of the annealing temperature.

Considering that the strain through the self-ordering process is related with the diffusion of residual Se atoms, we changed the amount of Se in each layer. Strains of samples with different compositions were measured by GIWAXS as shown in the figure below. Bi(3Å)/Se(5Å) has a d-spacing of 10.119 Å (strain of 6.029 %) and a Se-richer sample of Bi(3Å)/Se(13Å) has a d-spacing of 10.343 Å (strain of 8.383 %). This indicates that the amount of excess Se atoms affects strain through the self-ordering process. The strain of the sample is changed by around ± 1 % by controlling the amount of the Se atoms. However, for the Se-richer case (Bi(3Å)/Se(13Å)), the reflectivity line is broader than that for other cases, indicating that the Se-richer sample has a more rough surface morphology. Thus, we conclude that regulating strain by changing the Se composition also has limitations.

Since the lattice mismatch is dominant strain factor in general, we compared the strain with different substrates. We synthesized the films on a graphene substrate, because the the lattice mismatch between graphene and Bi2Se3 is about 3 %, resulting in tensile stress in in-plane direction of the film. We would also expect that the film would have a lower strain in the out-of-plane direction, compared to the film grown on Si. GISAXS measurements for Bi2Se3 films on the graphene substrate (below figures) show that, strain decreased from 3.88 % to 3.46 % for the 5QL samples and from 7.11 % to 5.07% for 3QL samples, compared to the film grown on Si. This shows the possibility of additional factors for controlling the substrate effect for the regulating the strain of the film. Since the synthesis method for the self-ordering process is based on a diffusion and reaction process, the induction of a large strain is indispensable. Although the strain is not perfectly controlled in the self-ordering process, it can be controlled to some degree.

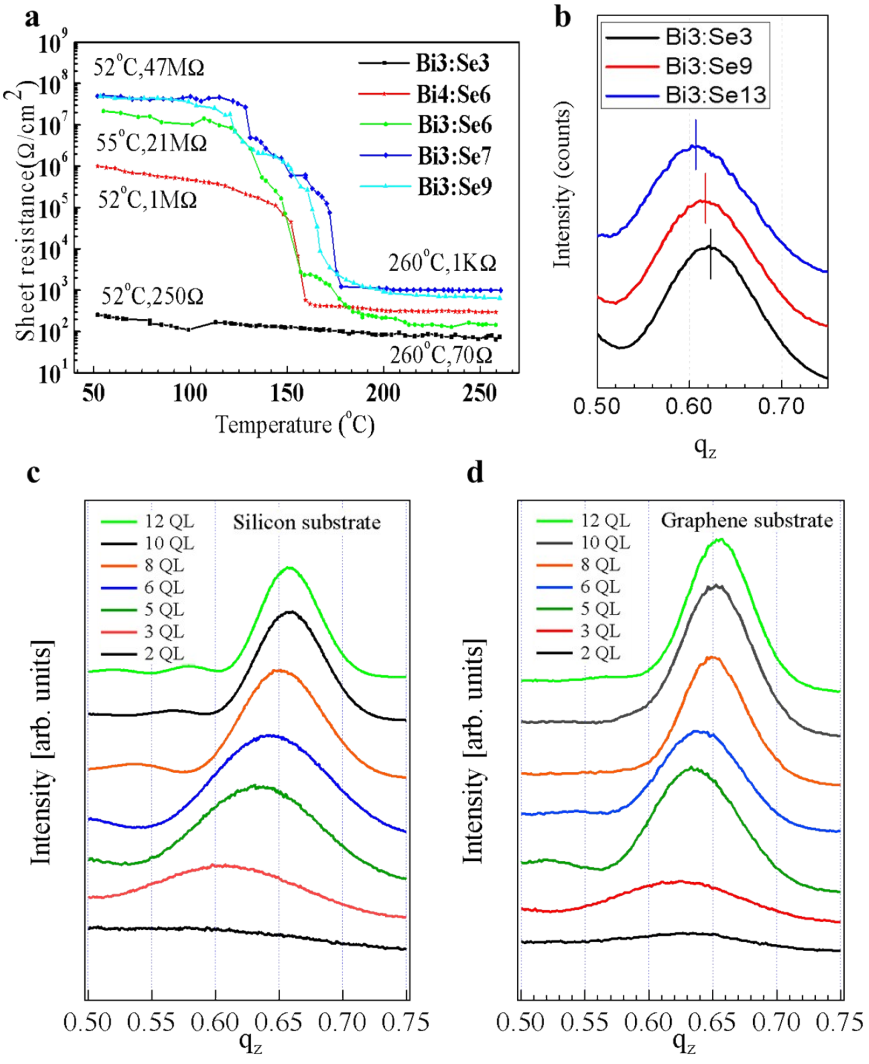

Figure S14 | a. Rs data for the Bi3Se9 b. out-of-plane scan profiles for the 3QL Bi2Se3 film of different as-grown composition obtained from the GISAXS patterns out-of-plan scan profiles for the Bi2Se3 films synthesized on Si substrate (c) and the graphene substrate (d)

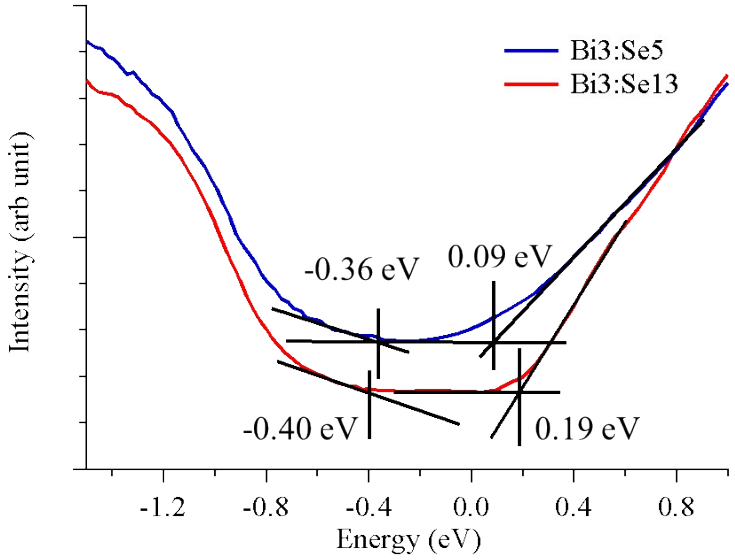

Figure S15 | Electronic structure measured by UPS and IPS for strain controlled Bi2Se3 with the same thickness.

In order to confirm the effect of strain on the band structure of Bi2Se3, we collected UPS and IPS data for two films with the same thickness and different strains. As shown in figure S13, the Bi3:Se5 and Bi3:Se13 3QL films, which have different strains, namely 6.029 % and 8.383 %, respectively. By this difference in strain, the band gap Valance band maximum is different by 0.04 eV and the conduction band minimum is different by 0.1 eV. By controlling growth condition we control bandgap of Bi2Se3 for 0.14 eV. This provides evidence for possibility of using strain in an engineered device.

S7. Weak Anti-localization effect in Bi_2Se_3 thin film.

We measure the Weak anti-localization effect of our 20 QL Bi_2Se_3 film by transport measurements. This is very important because the results indicate that thicker films behave like bulk topological insulator Bi_2Se_3.

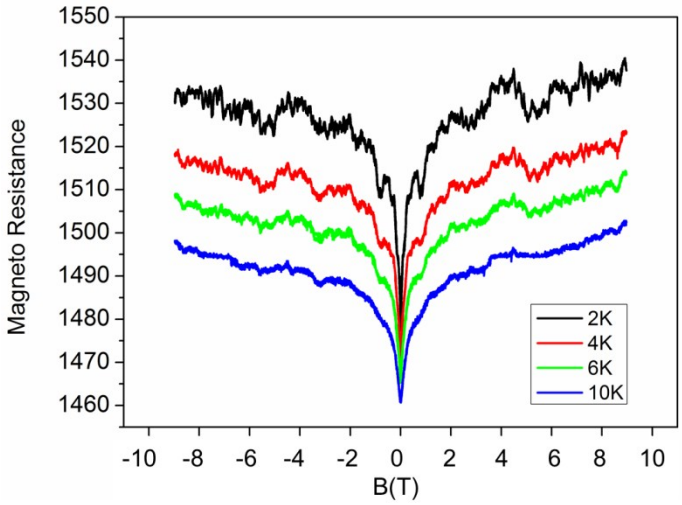

Figure S16 | Magnetoresistance showing weak-antilocalization effect on 20 QL Bi_2Se_3 film at 2~10 K.

References

1. T.-H. Kim, J. H. Baeck, H. Choi, K.-H. Jeong, M.-H. Cho, B. C. Kim and K. T. Jeong, *The Journal of Physical Chemistry C*, 2012, **116**, 3737-3746.
2. W. Dang, H. Peng, H. Li, P. Wang and Z. Liu, *Nano letters*, 2010, **10**, 2870-2876.
3. W. Richter and C. R. Becker, *physica status solidi (b)*, 1977, **84**, 619-628.
4. K. W. Adu, Q. Xiong, H. R. Gutierrez, G. Chen and P. C. Eklund, *Applied Physics A*, 2006, **85**, 287-297.
5. H. Richter, Z. P. Wang and L. Ley, *Solid State Communications*, 1981, **39**, 625-629.
6. J. Zhang, Z. Peng, A. Soni, Y. Zhao, Y. Xiong, B. Peng, J. Wang, M. S. Dresselhaus and Q. Xiong, *Nano letters*, 2011, **11**, 2407-2414.
7. W. Cheng and S.-F. Ren, *Physical Review B*, 2011, **83**.
8. Y. Yang, J. Y. Sun, K. Zhu, Y. L. Liu and L. Wan, *Journal of Applied Physics*, 2008, **103**, 093532.
9. M. Montazeri, M. Fickenscher, L. M. Smith, H. E. Jackson, J. Yarrison-Rice, J. H. Kang, Q. Gao, H. H. Tan, C. Jagadish, Y. Guo, J. Zou, M. E. Pistol and C. E. Pryor, *Nano letters*, 2010, **10**, 880-886.
10. D. Hsieh, Y. Xia, D. Qian, L. Wray, J. H. Dil, F. Meier, J. Osterwalder, L. Patthey, J. G. Checkelsky, N. P. Ong, A. V. Fedorov, H. Lin, A. Bansil, D. Grauer, Y. S. Hor, R. J. Cava and M. Z. Hasan, *Nature*, 2009, **460**, 1101-1105.
11. J. P. Perdew, K. Burke and M. Ernzerhof, *Physical Review Letters*, 1997, **78**, 1396-1396.
12. W. Cheng, L. Liu, P. Y. Yu, Z. X. Ma and S. S. Mao, *Annalen der Physik*, 2011, **523**, 129-136.

13. L. Fu and C. L. Kane, *Physical Review B*, 2007, **76**, 045302.
14. H. Zhang, C.-X. Liu, X.-L. Qi, X. Dai, Z. Fang and S.-C. Zhang, *Nat Phys*, 2009, **5**, 438-442.
15. H. Peelaers, B. Partoens and F. M. Peeters, *Nano Lett.*, 2009, **9**, 107-111.
16. !!! INVALID CITATION !!! {}.
17. S. Datta and B. Das, *Appl. Phys. Lett.*, 1990, **56**, 665-667.
18. P. D. C. King, R. C. Hatch, M. Bianchi, R. Ovsyannikov, C. Lupulescu, G. Landolt, B. Slomski, J. H. Dil, D. Guan, J. L. Mi, E. D. L. Rienks, J. Fink, A. Lindblad, S. Svensson, S. Bao, G. Balakrishnan, B. B. Iversen, J. Osterwalder, W. Eberhardt, F. Baumberger and P. Hofmann, *Phys. Rev. Lett.*, 2011, **107**, 096802.